Short Communication

Investigation of the Distribution of Temperature in the Electrochemical Machining Using Multiphysics Simulation

Hua Lin[1], Xiaochao Zhou[1,*], Changyong Cao[1], Gang Han[1], Meiyu Sha[1], Yubao Xu[2]

[1] School of Mechanical and Automotive Engineering, West Anhui University, Lu'an 237000, China
[1] School of Electrical and Photoelectronic Engineering, West Anhui University, Lu'an 237000, China
[*]E-mail: 39548804@qq.com

The distribution of temperature in the electrochemical machining (ECM) gap is uneven and it is hard to predict and measure it. In this paper, a multiphysics simulation model for the ECM temperature was established. The flow field and the temperature distribution in the gap were solved based on the turbulence model of Standard k-ε, Low Reynolds number (Re) k-ε, Shear stress transfer (SST), and Bubbly flow. The experimental device was built and the calculated and experimental results were compared. It was shown that the solution accuracy of the low Re flow model was higher than that of the high Re flow model. The computed temperature distribution obtained by employing the multiphysics model based on the low Re gas-liquid two-phase flow field was close to the experimentally measured one. This study could provide a basis for the accurate prediction of the anode profile of ECM.

1. INTRODUCTION

Due to the unique machining advantages, ECM is widely used in the precision machining of difficult-to-machine materials and complex surfaces in aviation, aerospace, weapons, and other fields [1-4]. The ECM process is a machining process under the comprehensive action of multiphysics. The uniformity of the temperature distribution in the electrolyte in the working gap has an important influence on the machining accuracy of the workpiece contour. Simulation technologies based on multiphysics coupling are widely used in the research of ECM to effectively improve the research and development efficiency [5-7]. Deconinck [8] studied the temperature distribution and the material removal law of ECM based on the laminar flow and multi-ion transport models. Klocke, et al. [9] used high-speed and thermography cameras to photograph the gas evolution and temperature development along the electrolyte channel and compared them with the simulation results obtained by employing the

multi-field coupling model using the bubbly flow model. Wang, et al. [10] carried out a numerical simulation on the multiphase flow field characteristics of the spiral deep hole ECM based on the mixture multiphase flow model. Zhou, et al. [11-12] conducted a multi-field coupling study on the ECM process of a blade surface based on the SST and Euler-Euler two-phase flow models. Chen and Fang, et al. [13-14] conducted the multi-field temperature simulation of high-frequency pulse ECM processes based on the k-ε model using the time-average quasi-steady-state algorithm. Lin, et al. [15-16] simulated the distribution of the gas volume fraction, the temperature, and the current density in the ECM of cross grooves using the turbulent k-ε and bubbly flow models.

There are many flow models for different research objects. The results of solving the flow field using different turbulence models and simulation parameters are not the same. In particular, the temperature results of multiphysics computations after coupling with the electric field and temperature field are different. Therefore, the temperature solution obtained by employing different flow models is important for the solution of the ECM multiphysics simulation model. In this study, the solution accuracy of ECM temperature will be improved by improving the solution accuracy of flow velocity in the near-wall region in the machining gap.

2. MULTIPHYSICS MODEL

In ECM, the anodic dissolution rate is directly influenced by the local current density. When the applied voltage is constant, the electric field in a machining gap is affected by the electrolyte conductivity and the geometry structure of the gap. The conductivity is affected by the temperature and the gas phase volume fraction and the temperature distribution is affected by the flow field and the electric field. So, the temperature distribution of ECM is the result of the joint action of multiphysics.

2.1 The geometric model

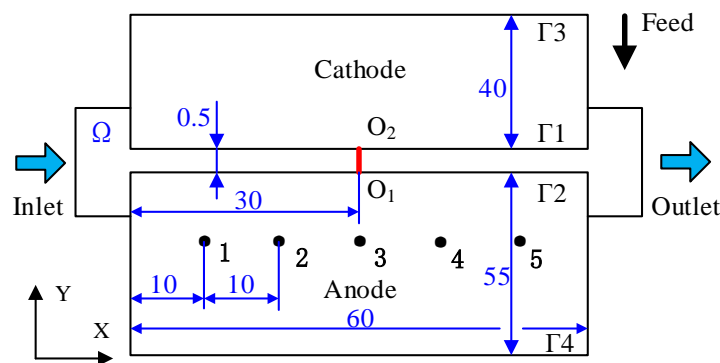The two-dimensional geometric model of planar ECM is shown in Figure 1.

Figure 1. Geometric model

The electrode thickness is 18 mm. The initial ECM gap is set as 0.5 mm, Ω represents the electrolyte region, 1~ 5 are the measuring points inside the anode, centerline O_1O_2 is used to observe the solution results in the gap.

2.2 The electric field model

In Figure 1, $\Gamma1$ and $\Gamma3$ are the cathode boundary, $\Gamma3=0$; $\Gamma2$ and $\Gamma4$ are the anode boundary, $\Gamma4=U$. In ECM, the mathematical model of the electric field can be found in reference [8]. The electrolyte conductivity in the machining gap is a function of temperature rise and gas-phase volume fraction, and its model cf. [8][15].

2.3 The turbulence model

In ECM, the electrolyte must have a certain speed and its flow state should be turbulent to discharge the heat and electrolytic products in time, and the flow field in the gap should be uniform to improve the machining accuracy. The high *Re* turbulence model such as the standard *k-ε* model, the low *Re* turbulence model such as the SST model, etc. are commonly used in ECM simulation. The electrolyte flow in the ECM gap satisfies the incompressible fluid Navier-Stokes equation.

$$\begin{cases} \rho \dfrac{\partial \boldsymbol{v}}{\partial t} + \rho(\boldsymbol{v}\cdot\nabla)\boldsymbol{v} = -\nabla p + (\mu + \mu_{\mathrm{T}})[\nabla\boldsymbol{v} + (\nabla\boldsymbol{v})^{\mathrm{T}}] \\ \rho\nabla\cdot\boldsymbol{v} = 0 \end{cases} \tag{1}$$

Where ρ is density; p is the pressure; $\boldsymbol{v}$ is the velocity; μ is dynamic viscosity; μ_T is turbulent viscosity.

In turbulence models, the general method of solving the flow velocity near the solid wall area there are two kinds of solving methods, one way is to introduce the wall function to establish the flow velocity equation in the boundary layer and the turbulent core region. Because this method is simplified the velocity calculation of the boundary layer, which greatly improved the calculation efficiency and convergence, and so, this method is applied widely in engineering simulation. But the model does not solve the flow in the buffer layer, therefore, the calculation accuracy of boundary layer velocity is not high. Another kind of method is to use the low Reynolds number model to solve the viscous bottom and transition layer, which has high accuracy in solving the flow velocity in the near-wall region, but the computational cost is relatively high, and the method is more difficult to converge when the model coupled with other physical models.

(1) Standard *k-ε* model

The standard *k-ε* turbulence model is a two-equation model and is a high *Re* flow model. The model needs to solve the velocity and length scale variables and uses the wall function to solve the near-wall velocity. The *k-ε* equations of the model can be expressed as [5][14],

$$\begin{cases} \rho \dfrac{\partial k}{\partial t} + \rho\boldsymbol{v}\cdot\nabla k = \nabla[(\mu + \dfrac{\mu_T}{\sigma_k})\nabla k)] + p_k - \rho\varepsilon \\ \rho \dfrac{\partial \varepsilon}{\partial t} + \rho\boldsymbol{v}\cdot\nabla\varepsilon = \nabla[(\mu + \dfrac{\mu_T}{\sigma_\varepsilon})\nabla\varepsilon)] + C_{1\varepsilon}\dfrac{\varepsilon}{k}p_k - C_{2\varepsilon}\rho\dfrac{\varepsilon^2}{k} \end{cases} \tag{2}$$

$$p_k = \mu_T \left[\nabla \boldsymbol{v} : (\nabla \boldsymbol{v} + (\nabla \boldsymbol{v})^T) \right] \tag{3}$$

$$u_T = \rho C_\mu \frac{k^2}{\varepsilon} \tag{4}$$

Where k is turbulent kinetic energy; ε is turbulent dissipation rate; p_k is the turbulent kinetic energy generated by the average velocity gradient; $C\mu$ is a standard constant. The model constant $\sigma_k = 1$; $\sigma_\varepsilon = 1.3$; $C_{1\varepsilon}=1.44$; $C_{2\varepsilon}=1.92$, respectively.

(2) Low Reynolds number k-ε model

At the location that is very close to the solid wall surface, the viscous effect of molecules is significant, the kinetic energy attenuation of turbulent pulsation is strong, and the dissipation rate reaches the maximum. To modify the standard k-ε model from the high Re region to the solid wall surface, the low Reynolds number k-ε model is obtained by introducing the correction term in the k-ε equations and modifying the C_μ, $C1\varepsilon$, and $C2\varepsilon$. There are many forms of the low Re k-ε model, cf. [17][18].

(3) SST k-ω model

The SST k-ω model is modified from the standard k-ω model. The k-ω model is suitable for the simulation of the near-wall low Reynolds number region. The SST k-ω model combines the advantages of the k-ω model in the inner boundary layer near the solid wall and the k-ε model in the high Reynolds number model in the outer fully developed turbulent region and has higher accuracy and reliability than the standard k-ω model. The model equations cf. [11][19].

(4) Turbulent bubbly flow

The models of multi-phase flow can be classified according to different scales, including the separated multi-phase flow and dispersed multiphase flow. The dispersed multi-phase flow mainly includes the bubbly flow model, mixed model, and two-fluid model. The fluid in the gap of ECM can be considered as a dispersed two-phase fluid with only hydrogen gas and electrolyte, the electrolyte is the continuous phase and hydrogen is the dispersed phase. In this paper, the turbulent bubbly flow model is used for calculation and analysis. The specific model equation can be referred to in the literature [13][15].

2.4 The thermal model

The resistance of the electrode is so small that the joule heat generated during ECM can be ignored. The heat can be considered to be composed of the joule heat of electrolyte and the electrochemical reaction heat at the boundary of electrode and electrolyte. The cathodic boundary Γ3 and anode boundary Γ4 are assumed to be naturally convective with air, and other boundaries are thermally insulated. The temperature distribution of the electrolyte can be described by the convection-diffusion equation [14],

$$\rho c_p \frac{\partial T}{\partial t} + \rho c_p \boldsymbol{v} \cdot \nabla T = \nabla \cdot (k_t \nabla T) + \kappa (\nabla U)^2 + U_k i_k \tag{5}$$

In which, c_p is the specific heat capacity of electrolyte at atmospheric pressure, k_t is the thermal conductivity of the electrolyte, U_k is the overpotential, i_k is the local current density.

2.5 The simulation process and parameters

The geometric model (Figure 1) was drawn in *AutoCAD* and then imported into the multi-physics software *COMSOL Multiphysics* (version 5.6) for the solution. The Physical field modules of turbulent and turbulent bubbly flow, the electric field of primary current, fluid heat transfer were added. After the boundary conditions and the parameters were set, the meshing was operated. The transient solver was selected. The solver tolerance was set as 0.01, the solution time step was set as 0.01s. The solution process of the multiphysics coupling temperature simulation model of ECM is shown in Figure 2. The initial values and ECM parameters in the model are shown in Table 1.
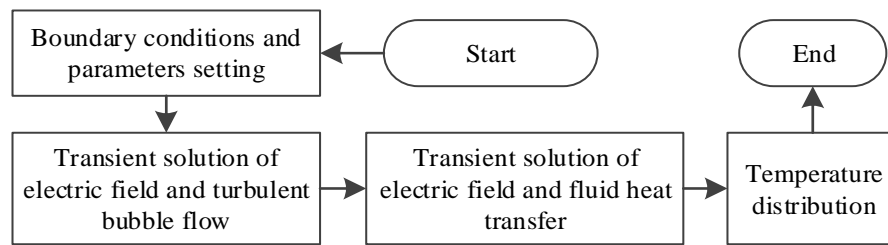

Figure 2. Flow chart of multiphysics coupling model solution

Table 1. Anode, cathode, and electrolyte initial values and ECM parameters

Parameters	Value
Initial conductivity of electrolyte k_0/(S/m)	7.2
Electrolyte density ρ_l/(Kg/m^3)	1053
Specific heat capacity of electrolyte c_{pl}/[J/(kg·K)]	3730
The electrolyte initial temperature T_0/(K)	298.15
Inlet velocity p_i/(MPa)	0.3;0.35
Outlet pressure p_o/(MPa)	0;0.18
Hydrogen molar mass M_{H2}/(g/mol)	2
Electrode density ρ_s/(Kg/m^3)	7930
Electrode thermal conductivity k_t/[W/(m·K)]	15.2
Specific heat capacity of electrolyte c_{ps}/[J/(kg·K)]	500
Applied voltage U/(V)	20
Cathode feed velocity v_c /(mm/min)	0.3

As seen in Figure 2, the indirect solution method was adopted in consideration of the need to calculate the numerical stability and efficiency of the multi-physical model. The transient solution of the electric field and the flow field is carried out simultaneously to obtain the gas phase volume fraction (bubble rate) and the distribution of current density that is affected by bubble rate, and then the results

are passed to the next transient solver for simultaneously compute the electric field and fluid heat transfer. Finally, the temperature distribution in the ECM gap is obtained.

3. SIMULATION RESULTS AND ANALYSIS

The temperature distribution in the gap is the result of the interaction of multiphysics. The flow field distribution, especially the flow field distribution near the wall has a great influence on the heat transfer effect and the temperature distribution. The flow field is mainly reflected in the distribution of the bubble rate and the current density, and this ultimately affects the solving accuracy of the ECM simulation model. In this section, the flow field and the temperature distribution in the gap are solved and discussed based on the different turbulence models coupled with the electric field and the temperature field.

3.1 Flow velocity distribution

The solution of the flow velocity is an important step in solving the heat transfer in ECM. Set the inlet pressure of the model as 0.3 MPa and the outlet pressure as 0 MPa. The velocity distribution in the gap is calculated by the turbulence standard k-ε, low Re k-ε, and SST, respectively. The flow velocity distribution of centerline O_1O_2 is shown in Figure 3.
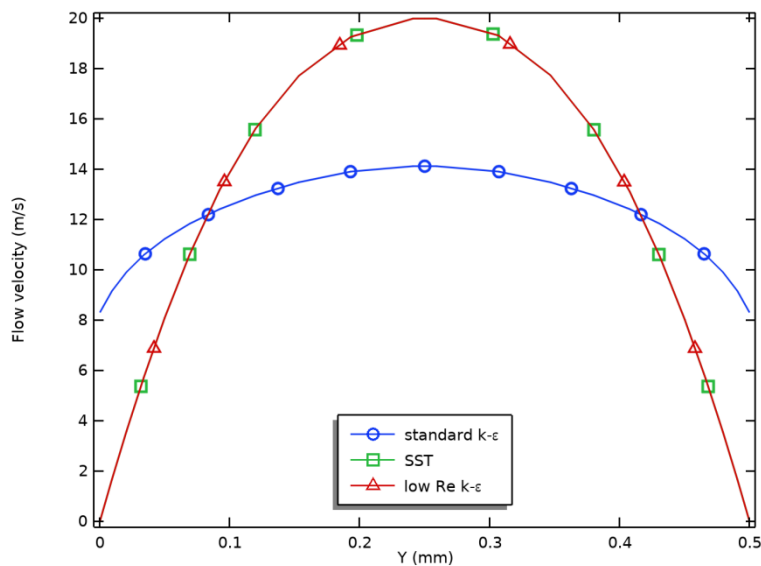

Figure 3. Flow velocity distribution of centerline O_1O_2 under different turbulence models

It can be seen from Figure 3 that the solution results of the turbulence models were different and the flow velocity was the largest at the midpoint of the gap. The calculated value using the standard k-ε model was nearly the averaged one and the calculated values using the SST and low Re k-ε models were almost the same. The central gap velocity value calculated by employing the standard k-ε model was smaller than that calculated by employing the other two models. The flow velocity in the near-wall region solved by employing the standard k-ε was the highest and its lowest velocity was 8.3 m/s.

However, the velocities obtained by employing the SST and low *Re k-ε* models were from 0 m/s (at the solid wall) to 20 m/s (in the center of the turbulent flow).

These conclusions mentioned above are consistent with the conclusions in reference [20], in which the author pointed out through comparative study of numerical computation and experiment that the selection of turbulence model has a great influence on the numerical calculation, and the simulation accuracy of the near-wall region with low *Re* model is higher.

In the simulation, the use of the low Reynolds number model to improve the accuracy of the solution of the flow field near the wall enhanced the reliability of the temperature results. Thereby, the accuracy of the ECM multiphysics model was improved. The following temperature computation and analysis were conducted based on the low *Re k-ε* model.

3.2 Temperature distribution

The velocity distributions obtained by employing different flow models are different and the temperature distributions based on different velocity distributions are also different. Therefore, the improvement of the accuracy in solving the flow field near the wall will improve the accuracy in solving the temperature distribution. This will improve the accuracy in solving the conductivity and the current density and finally improve the accuracy in solving the multiphysics model of ECM.

In ECM, the Joule heat is generated in the working gap. Therefore, a lot of hydrogen bubbles are generated near the cathode followed by the high-velocity movement of the electrolyte toward the outlet. The higher the flow velocity is, the more heat and bubbles are taken away and the lower the temperature rise along the flow path is. At the same time, the generation and transport of bubbles also affect the generation and conduction of heat.

In the gas-liquid two-phase model, other gases are ignored and the cathode boundary $\Gamma 1$ is set as the hydrogen gas inlet, where the mass flux is[17]:

$$N_{\mathrm{H}} = M \frac{\eta i}{2\mathrm{F}} \tag{6}$$

In which, $\eta=1$; N_H is hydrogen flux; M is the molar mass of hydrogen; F is Faraday's constant.

Set the inlet pressure as 0.3 MPa, the outlet back pressure as 0 MPa, the voltage as 20 V, and the processing time as 1 s. Based on the turbulence standard *k-ε* and low *Re k-ε* model and the low *Re k-ε* model coupled with the bubbly flow model, the temperature distribution of centerline O_1O_2 in the ECM gap is solved, and the temperature on centerline O_1O_2 is shown in Figure 4.

The similar simulation results can be seen in the reference [11] and [21]. The simulation and experimental study in the reference [11] shows that the ECM temperature calculated by the Euler-Euler two-phase flow model was closer to the experimental result than that calculated by the *k-ε* model. Luo [21] pointed out that the heat transfer calculation results of the low Reynolds folw model of *k-ω* and SST *k-ω* for turbine guide blades had little difference from the experimental results, and its accuracy was higher than that obtained by employing the *k-ε* and *RNG k-ε* models. Therefore, the ECM multiphysics temperature distribution simulation model based on the low *Re k-ε* coupled with the bubbly flow has higher accuracy.
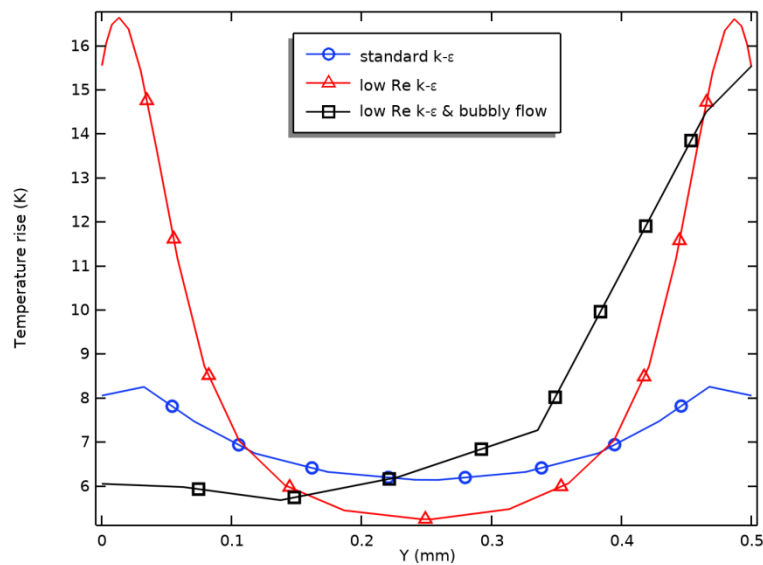
Figure 4. Temperature distribution of centerline O_1O_2 under different turbulent flow models

It can be seen from Figure 4 that the temperature distributions obtained by employing different turbulence models are not the same. In the range of 0 ~ 0.1mm near the electrode wall, the temperature rise solved by employing the low *Re k-ε* model was larger than that by employing the standard *k-ε* model. The temperature rise near the anode wall differed by 8 K. This was because the low *Re k-ε* model accurately solved the flow velocity near the wall. Its value was smaller than that obtained by employing the standard *k-ε* model using the wall function. It is known that a larger flow velocity can take away more heat from the machining region within the same time.

The calculated temperature rise near the anode based on the low *Re k-ε* model coupled with the bubbly flow model was relatively small and that at the cathode was the largest. The main reason was that the bubbles were generated and accumulated near the cathode. The two-phase flow velocity was very low near the cathode wall and the heat taken away was small. So the temperature rise was relatively significant and more heat could be transferred to the cathode.

4. EXPERIMENTAL RESEARCH

4.1 Experimental device and processing parameters

To verify the influence of different turbulence models on the solution of ECM temperature, a comparative study of simulation and experiment was carried out. The experimental device is shown in Figure 5.

As shown in Figure 5, the stainless steel anode was fixed on the worktable of the ECM machine tool. The cathode was fixed on the Z-axis. The electrolyte was pumped into the inlet of the experimental device and the inlet and outlet pressures could be varied by rotate the valve and could be displayed on the pressure gauge. These parts were well sealed to prevent leakage of the electrolyte.
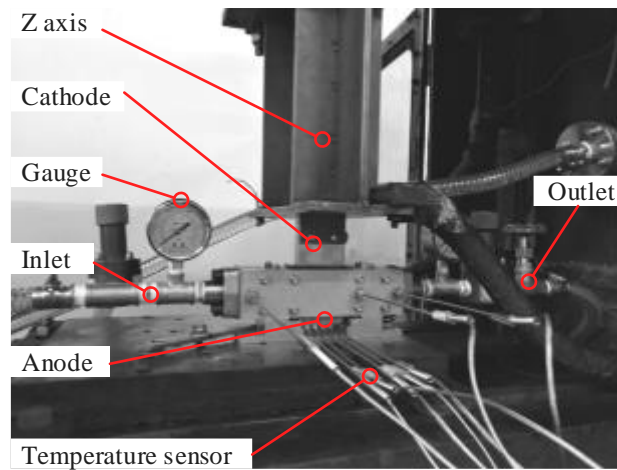
Figure 5. Experimental device

Since it was difficult to directly measure the temperature in the gap of ECM, the indirect temperature measurement was carried out by installing temperature sensors in the anode machining holes, and the temperature signal of each sensor was processed by the STM32 embedded system [22].

The simulation and experiment processing parameters were; the inlet pressure was 0.35 MPa, the outlet back pressure was 0.16 MPa, the initial electrolyte temperature was 28°C, the processing voltage was 20 V, the electrolyte was 8wt% $NaNO_3$, the cathode feed speed was 0.3 mm/min, and the processing time was 400 s.

4.2 Results and discussion

In the simulation, the flow model selects the low *Re k-ε* model and coupled bubbly flow model, and the contour map of temperature distribution at 400 s is shown in Figure 6, and the temperature rise change data at points 1 to 5 are shown in Figure 7. The simulated temperature rise value and the experimental measurement data of points 1~ 5 at 400 s in the anode are shown in Figure 8.

It can be seen from Figure 6 that the heat transfer gradient in the cathode was larger. The temperature rise was larger near the outlet and the maximum temperature rise was 55 K in the latter half of the gap. This was mainly because that the two-phase flow velocity near the cathode was relatively small and the accumulation of heat and bubbles along the flow path was significant. The heat transfer gradient in the anode was relatively small because the bubble volume fraction near the anode boundary was relatively small and the flow velocity was relatively large. So more heat was carried away by the electrolyte (Figure 4) and the heat transferred to the anode was comparatively small.
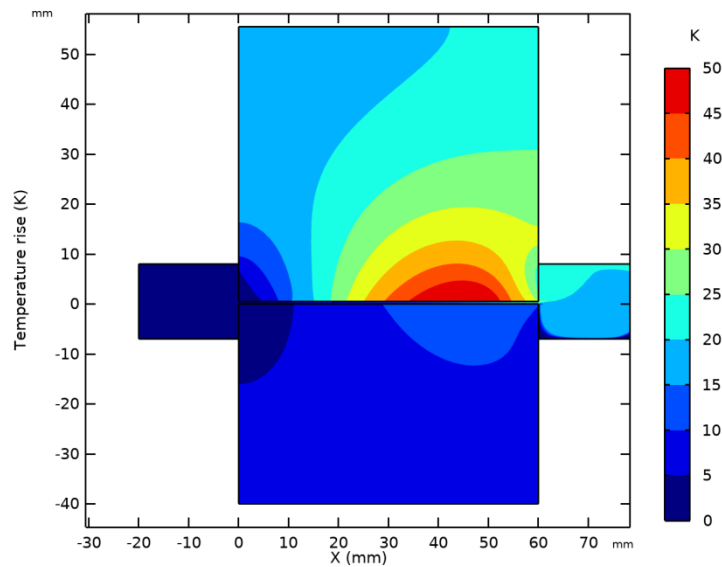
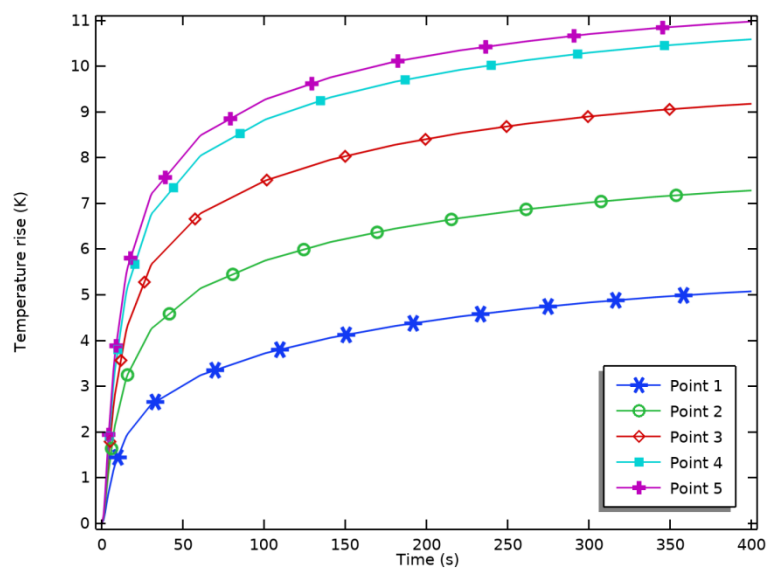**Figure 6.** Figure of temperature rise distribution

Figure 7. Temperature rise simulation value of points 1 ~ 5

It can be seen from Figure 7 that, due to the accumulation of heat, the temperature rise at the measurement points 1 to 5 increased sequentially and the temperature rise difference between points 4 and 5 was relatively small. It was because that the back pressure was 0.18 MPa and more heat accumulated in the latter half of the ECM gap. Also, it can be seen that, as the processing progressed, the temperature at each point gradually increased. The temperature increased rapidly during the time of 0 ~100 s and entered a dynamic quasi-steady-state at about 200 s. After that, the temperature increase slowed down. The temperature rise at point 5 finally stabilized at about 10.9 K.
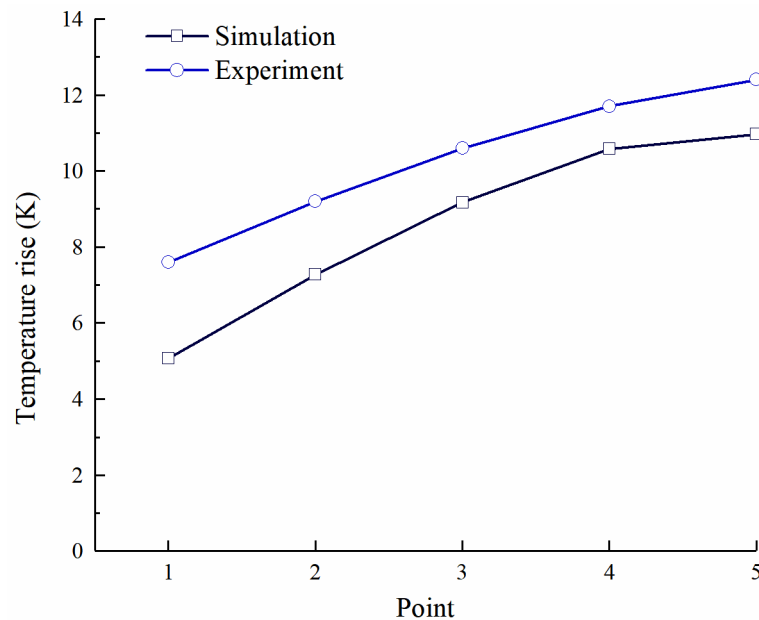
Figure 8. Comparison of simulation results and experimental measurement data at point 1 ~ 5

As can be seen in Figure 8, the simulated growth trend of the temperature rise was consistent with the measured experimental results. The temperature rise difference between points 5 and 1 along the flow channel was almost equal to the experimental value (about 5.8 K). The temperature rise measured in the experiment was generally larger than that obtained by the simulation and the difference in the steady-state temperature rise at point 5 was about 1.5 K. The main reason was that the heat exchange between the electrode and the outside in the simulation model was set as the natural convection by air. But the electrode was fixed in the tooling which was fixed to the machine tool in the experimental device. So the thermal conductivity in the boundary layer was larger than the natural convection by air. Another reason was that the two-dimensional simplified model used in the simulation in this paper could not fully reflect the actual ECM situation, especially the solid heat transfer process in the anode with holes for installing the sensors inside. Therefore, the difference between the simulated temperature in the electrode and the experimentally measured temperature was small.

5. CONCLUSIONS

(1) There was a big difference in the solution accuracy in the near-wall region among different turbulence flow models. The low Reynolds number flow model could solve the flow velocity in the boundary layer with higher accuracy than the high Reynolds number model. The SST flow model and the low *Re k-ε* model showed similar calculated results.

(2) The gas-liquid two-phase bubbly flow model based on the low Reynolds number flow model predicted a lower calculated temperature value near the anode than that obtained by employing the single-phase flow model.

(3) The multiphysics ECM model based on the low *Re* gas-liquid two-phase flow model showed high accuracy in the temperature solution and its solution was well consistent with the actual situation.

When the model will be applied to the prediction of the ECM workpiece contour, the prediction accuracy is expected to be improved.

References

1. Y. L. Chen, P. X.Chen, H. Lin and X. Li, *Int. J. Electrochem. Sci.,* 15 (2020) 10955.
2. Z. Y. Xu, L. Y. Sun, Y. Hu and J C Zhang. *Int. J. Adv. Manuf. Technol.*, 71 (2014) 459.
3. X. Z. CHEN, Z.Y. XU, D. Zhu, Z. D. Fang and D. Zhu, *Chinese. J. Aeronaut.*, 1 (2016) 274.
4. T. Fujisawa, K. Inaba, M. Yamamoto and D. Kato, *J. Fluid Eng.,* 130 (2008).
5. D. Zhu, J. C. Zhang , K. L. Zhang, J. Liu, Z. Chen and N. S. Qu, *Int. J. Adv. Manuf. Technol.*, 80 (2015) 637
6. F. Klocke, M. Zeis, S. Harst, A. Klink, D. Veselovac and M. Baumgärtner, *Procedia CIRP,* 8 (2013) 265.
7. S. Hinduja and J. Pattavanitch, *CIRP J. Manuf. Sci. Tec.,* 12 (2016) 79.
8. D. Deconinck, S. V. Damme, C. Albu, L.Hotoiu and J.Deconinck, *Electrochim. Acta,* 56 (2016) 5642.
9. F. Klocke, M. Zeis and A. Klink, *CIRP Annals,* 64 (2015)217.
10. M. H. Wang, W. S. Liu and W. Peng, (2013). *Acta Armamentarii,* 34 (2013) 748. (In Chinese)
11. Y. L. Chen, X. C. Zhou, P. X Chen and Z. Q. Wang, *Chinese. J. Aeronaut.*, 33 (2020) 1057.
12. X. C. Zhou, C. Y. Cao, H. X. Wang and H. Lin, *Int. J. Adv. Manuf. Technol.*, 109 (2020)1655.
13. M. Fang, Y. L. Chen, L. J. Jiang, Y. S. Su and Y. Liang, *Int. J. Adv. Manuf. Technol.*, 105 (2019) 3261.
14. Y. L. Chen, M. Fang and L. J. Jiang, *Int. J. Adv. Manuf. Technol.,* 91 (2017) 2455.
15. H. Lin, Y. L. Chen, X. Li, H. G. Li and Q. Chen, *Int. J. Electrochem. Sci.,* 16 (2021) 150959
16. Y. L. Chen, H. Lin, B. Cai, and Q. Chen, *Int. J. Adv. Manuf. Technol.*, 2021. https://doi.org/10.1007/s00170-021-07958-8
17. L. Ignat, D. Pelletier and F. Ilinca, *Comput. Method Appl. M.,* 189 (2000) 1119
18. K. Abe, T. Kondoh and Y. Nagano, *Int. J. Heat Mass Tran.,* 37 (1994) 139.
19. F. R. Menter, *24th fluid dynamics conference,* AIAA (1993) 2906.
20. H. M. Ma, H. P. Chen, M. Su, X. Bai, G. Xu and Y. F. Liu, *Journal of Shanghai Jiaotong University,* 40 (2006) 326. (In Chinese)
21. J. X. Luo, H. R. Zhu and Z. W. Zhang. *Journal of Aerospace Power,* 29(2014):526. (In Chinese)
22. Z. Q. Wang, X. C. Zhou and H. Lin. *Instrument Technique and Sensor,* 9 (2019) 23. (In Chinese)